Liquids with conics

M. Kleman [a]; O. D. Lavrentovich [b]

[a] Institut de Physique du Globe de Paris, France [b] Liquid Crystal Institute and Chemical Physics Interdisciplinary Program, Kent State University, Kent, Ohio, USA

PLEASE SCROLL DOWN FOR ARTICLE

INVITED ARTICLE

Liquids with conics

M. Kleman[a]* and O.D. Lavrentovich[b]*

[a]*Institut de Physique du Globe de Paris, 4, place Jussieu 75252 Paris cédex 05, France;* [b]*Liquid Crystal Institute and Chemical Physics Interdisciplinary Program, Kent State University, Kent, Ohio 44242, USA*

A red thread marks the history of liquid crystals from the start; it is the concept of focal conic domains in smectic phases. Discovered by G. Friedel and F. Grandjean early in the beginning of the 20th century, focal conic domains still attract the attention of researchers in the field. The presence of focal conic domains is a touchstone of layered media. They rightly excited the interest of P.-G. de Gennes in a seminal paper about the Apollonius tiling of toric focal conic domains. In this paper we shall review the development of this notion over the last one hundred years, firstly emphasising its importance in the appearance and broadening of the concept of order and of its singularities in liquid crystals and beyond in condensed matter physics, through the renewed notions of dislocations, disclinations, grain boundaries, kinks and focal conic domain imperfections, then describing the empirical evidence of focal conic domains in various liquid crystalline materials, and finally how they have inspired research in visualisation methods and molecular architectures.

Keywords: Smectic A; focal conic domains; disclinations; kinks; double helices; 3D microscopy

1. Introduction

The history of liquid crystals (LCs) starts with the discovery that certain liquids are birefringent and display figured elements that do not break the continuous liquid character of the phase, easily change shape and size, easily disappear or multiply, and depend on static and dynamic boundary conditions. These elements, later called defects or singularities, appear under different aspects in different liquid crystalline phases; indeed their observation in polarising light microscopy allows for a characterisation of the liquid crystalline phase, whether it is nematic, cholesteric, smectic, columnar, etc. Lamellar phases from that point of view are very easy to identify, thanks to the presence of macroscopic line defects (whose size in general scales with the size of the sample), such as oily streaks, focal conic domains (FCDs), double helices (DHs), etc. Among this set of macroscopic objects the *FCDs* are particularly remarkable by the presence of conics (an ellipse and a hyperbola going in pairs, as it was soon recognised). These conics may look perfect in smectic A phases (SmAs), at least in current light microscopy observations (Figure 1(a)) or present imperfections that in some circumstances can be analysed in geometric terms. Other lamellar phases, liquid like smectic C phases (SmCs), or with a layer of partial two-dimensional ordering, such as smectic B (SmB), show up similar figures, but broken in specific

ways. This paper will concentrate on FCDs and their interplay with other defects in a SmA.

Lehmann (*1, 2*) was the first to attach importance to defects in LCs; he not only described them in great detail with the purpose of correlating them to the molecular structure, but he also advanced that some of them are related to primitive aspects of life, in particular the very mobile SmA nuclei that appear at the transition from an isotropic phase to a SmA phase (Figure 1(b)). However, the true physical characteristics of these nuclei, in no way indicative of life, were first cleared up by Friedel and Grandjean (*3*); these *bâtonnets* (rod-like formations), as they called them, are made of conjoint domains bordered by paired conics. Such domains persist in the bulk when the transition to the SmA phase is completed. In an article – *Liquides á coniques focales* – whose title we have borrowed for the present paper, they related the existence of these conics and the domains they border to large scale arrangements where the layers conserve *perfect parallelism*, but are allowed to curve (*3*). This condition provides a guide in the analysis of a whole family of defects, as follows.

1.1 Focal conic domains

A well-known result concerning a family of parallel surfaces, S_i, is that their normals envelop two *focal* surfaces, F_1 and F_2, which are the loci of the centers of

---

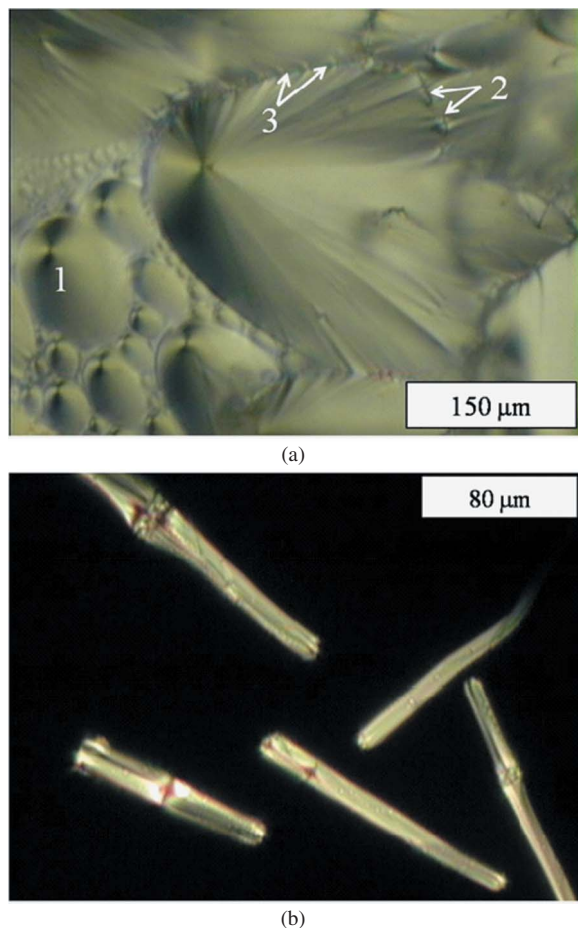*Corresponding authors. Email: maurice.kleman@mines.org and odl@lci.kent.edu

(a)

(b)

Figure 1. Polarised light microscopy: (a) FCDs in a thick (120 μm) sample of dodecylcyanobiphenyl (12CB) – notice FCDs of different orientation, with ellipses parallel to the plane of view (1), ellipses perpendicular to the plane of view (2,3) and FCDs forming a grain boundary (3); (b) SmA bâtonnets nucleating from the isotropic phase, on which small FCDs are visible.

curvature C_1 and C_2, common at all the surfaces along a common normal (Figure 2(a)). If these S_is are SmA layers, their normals carry the molecular directions **n**. The curvature |div**n**| is infinite at C_1 and C_2; F_1 and F_2 are thus singularities of the director field, where the smectic order parameter is broken, and the energy attached to these singularities necessarily scales as the area of F_1 and F_2. It is therefore reasonable that small energy parallel arrangements are such that the focal surfaces are degenerated to lines. However, it can be demonstrated that these *focal lines* form a set of two *conjugate conics* (i.e. an ellipse and a branch of hyperbola in two orthogonal planes, such that the apices of one are the foci of the other). The layers take the shape of *Dupin cyclides* (Figure 2(b)) (for a good qualitative presentation of these surfaces, see (*4*)).

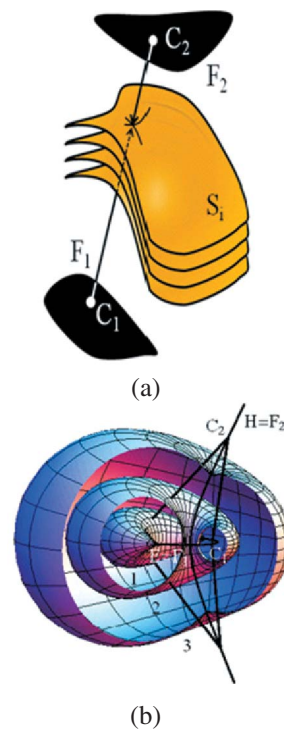The geometric regularity and beauty of these FCDs has attracted the attention of a number of researchers,

(a)

(b)

Figure 2. (a) Schematic representation of a set of parallel surfaces S_i, their normals, and the loci of the centres of curvature C_1 and C_2, the focal surfaces F_1 and F2; (b) F_1 and F_2 degenerated into two conjugate conics *E* (ellipse) and *H* (hyperbola). The straight lines are normals to the cyclides. Numbers 1, 2, and 3 label three different types of Dupin cyclides: with cusps at the ellipse (1), cusp-free (2), and with cusps at the hyperbola (3).

e.g. Friedel (*5*), Bragg (*6*), Chystiakov (*7*), Bouligand (*8*) and cf. (*9*) for a historical review with emphasis on the work of G. Friedel. In this vein, Bidaux *et al*. published a seminal paper in 1973 (*10*) about the Apollonius packing of *toric* FCDs (TFCDs). Such arrangements, where the ellipse is reduced to a circle, the hyperbola to a straight line, passing through the centre of the circle, and the Dupin cyclides to tori, has been observed in several circumstances, e.g. in a Lα phase (*11*). This will be discussed in Section 3.

There are several types of FCDs, depending on the sign of the Gaussian curvature of the layers. Figure 3 represents the different cases, which are explicited in the caption. Take a straight line joining any point *M* on the ellipse to any point *P* on the branch of the hyperbola; by the very definition of a normal to a set of parallel surfaces, the infinite line $L = MP$ is such a normal. However, passing to the interpretation of *L* as a base for the director, it appears visible that the three segments into which it is divided (the finite segment *MP* and the two outside half-infinite lines M∞ and P∞) are orthogonal at a point $Z \in L$ to layers of opposite Gaussian

curvatures $G = 1/\sigma_E \sigma_H$, $(\sigma_E = 1/ZM, \sigma_H = 1/ZP)$, namely G is negative for Z between M and P, positive outside. Empirically it is observed that the vast majority of FCDs are made of layers of *negative Gaussian curvature*; this condition restricts the layers to the inner part of two half cylinders symmetrical with respect to the plane of the ellipse, as in Figure 3(a) (complete ideal FCD of type I). Figures 3(b) and 3(c) represent FCDs with positive G of layers. The geometry of Figure 3(b)
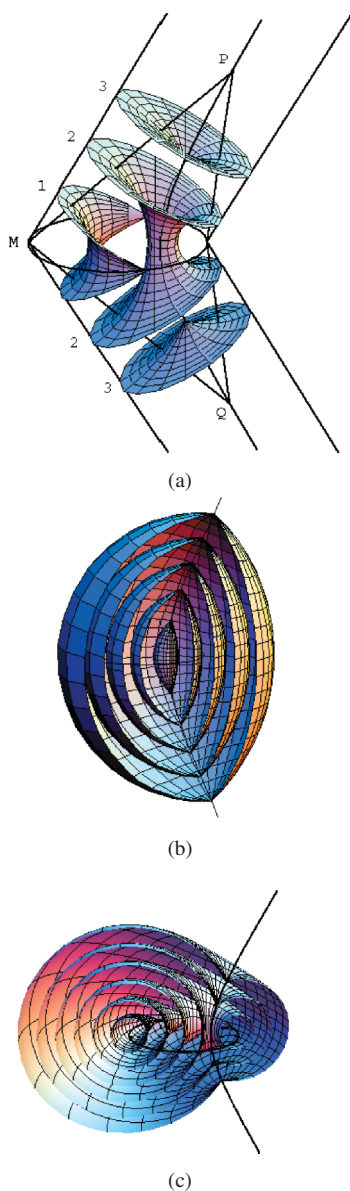

(a)

(b)

(c)

Figure 3. (a) Complete FCD of type I; the layers are restricted to their negative Gaussian curvature parts – notice that they can be prolongated outside the domain by planar layers that have to meet in the region of the plane of the ellipse (see Section 3); (b) FCD of type II, layers of positive Gaussian curvature – notice that the ellipse does not appear as a singular line; (c) the presence of both positive and negative Gaussian curvature layers.

has been observed in a lyotropic $L\alpha$ phase (*12*). A detailed description can be found in (*13*).

Of course, since the layers of a FCD are parallel, the main energy contribution is curvature energy.

Two final remarks: (i) the limiting case of FCDs of vanishing eccentricity $e = 0$ are TFCDs. FCDs of unit eccentricity, $e = 1$, made of two conjugate parabolae (*14*), have a small curvature energy per unit volume and are very frequently observed; (ii) the layer parallelism condition is not observed in the core regions of E and H, which are singular regions (*15*).

1.2 Small Burgers vector dislocations

Whereas FCDs are mostly macroscopic, visible objects, there are, at the other extreme, dislocations of *small* Burgers vector b (Figure 4); *small* means here that b is comparable to the SmA repeat distance d_0, so that they are not visible in polarising light microscopy. Dislocations of small b do not fulfil the condition of parallelism of the layers, which is central in the stability of FCDs. This is a field in which de Gennes has also been active; he gave the first calculation of the layers profile and energy of an edge dislocation, using a linearised version of SmA elastic free energy density (*16*). At such small scales, it is important to take into account the strain energy, which may balance the curvature energy. Recent developments account for a non-linear term in the strain energy (*17, 18*) that leads to pronounced experimentally observed features of layer distortions around the edge dislocation (*19*).

1.3 A classification of line defects in a SmA

In-between dislocations at molecular scales and ideal FCDs, one finds a menagerie of various defects, characterised by various levels of interplay
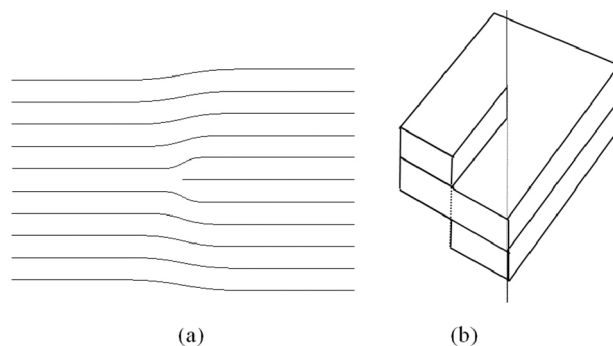

(a)   (b)

Figure 4. (a) Cross section of an edge dislocation, the Burgers vector is perpendicular to the line; (b) screw dislocation, the Burgers vector is parallel to the line.

between dislocations of a small Burgers vector and FCDs at different scales. These are:

– Clusters of parallel edge dislocations, also called *oily streaks*. These oily streaks, when *b* is large enough (in fact macroscopic, it can be as large as several thousands repeat distances), split into FCDs in contact along their ellipses (*20*).
– Clusters of parallel screw dislocations, which recompose into an attached sequence of distorted partial focal conics, forming DHs (*21*). They are described in Section 2.3.
– Clusters of FCDs forming tilt grain boundaries (*10, 22*). They are discussed in Section 3.

1.4   Volterra process and topological defects

We refer the reader to (*23*) and (*24*) for a full presentation of the Volterra process (VP), by which it is possible to construct all the line defects of an ordered medium with the sole recourse to its properties of symmetry in its ground state. However, a detailed knowledge of the VP is not necessary here. We recall that *dislocations* (they break translational symmetries (*23*)) and *disclinations* (they break rotational symmetries (*24*)) can be treated as Volterra defects. Frank's renowned paper (*25*) introduces the notion of disclination in nematics as resulting from a VP; he used at that time the word *disinclination*. Insofar as a disclination breaks the rotational symmetries of the director field of a LC, there is no difference in definition between a disclination in a nematic and in a SmA, since the director fields are similar. The differences come from the elastic properties, which are drastically different, due to the presence of layers in a SmA.

The FCD ellipse and hyperbola are special *disclinations*. Indeed, choose any point on the hyperbola, the director is rotated by an angle of 2π about the tangent to the hyperbola at this point; choose any point on the ellipse, the director is rotated by an angle $\Omega = \pi$ about the tangent **t** to the layer at this point (see Figure 11, Section 3.2). However, their construction through the VP is revealed to be impossible, at least for the ellipse. This is because of the subtle properties of interaction between the dislocations and disclinations. The solution is in an *extended VP*, whose essentials are discussed in Section 2.2.

2.   Interplay between focal conic domains and dislocations: elasticity, kinks

The interplay between FCD disclinations (*E* and *H*) and dislocations involves: i) the *elastic properties* of a SmA, and ii) the *extended Volterra* properties of the partners in interaction, which is captured in the notion of *kink*. The extended VP also embraces the description of the relaxation of all the deformations that do not contribute to the energy in Equation (1), e.g. the easy glide of layers one past another. In terms of VP, these deformations can be attributed to the interaction of continuous dislocations with a disclination (*26*). Disclinations and dislocations are present in all LC phases, so this notion is rather general. Its study does not require the use of the rather highbrow concepts of the *algebraic topology of defects* (*13*); a more elementary geometric approach akin to the VP will serve our purpose (*26*).

2.1   The elasticity of defects in a SmA phase

We make the differences between the small and large scales we have introduced above explicit. The two contributions – *strain* elasticity, i.e. the compressibility of the layers, *curvature* elasticity, i.e. the curvature of the layers – have different ranges of action. Let *R* be the typical size of a domain submitted to some compression or tension: the strain energy scales as $F_{strain} \approx BR^3$, the curvature energy as $F_{curv} \approx KR$. *B* and *K* are the classic moduli of the free energy density

$$f = \frac{1}{2} K (\mathrm{div}\, \mathbf{n})^2 + \frac{1}{2} B \left(1 - \frac{d}{d_0} \right)^2 + \bar{K} \sigma_E \sigma_H, \quad \lambda^2 = \frac{K}{B}, \quad (1)$$

where $\mathbf{n}(x,y,z)$ **is** the director, $d(x,y,z) > 0$ the thickness of the deformed layer, and λ a material length that cannot be much different from d_0, the thickness of an unperturbed layer. The term $\bar{K}\sigma_E\sigma_H$ ($\bar{K}$ is the *saddle-splay* modulus) can be integrated to a surface term and should be considered whenever the topology of layers is altered; this is precisely the case of layers in FCDs as compared to flat layers. The ratio $F_{strain}/F_{curv} = (R/\lambda)^2$ is much larger than unity as soon as $R > \lambda$. Therefore, the only distortion of a macroscopic medium should be curvature: the layers with vanishing strain are parallel. On the other hand, at small scales, the strain energy and the curvature energy can balance. Another remark, which later will prove important, is that the curvature contribution of a layer with vanishing mean curvature (a minimal surface) vanishes: $\mathrm{div}\,\mathbf{n} \equiv \pm (\sigma_E + \sigma_H) = 0$ (this is the case when a layer takes the shape of a *ruled helicoid* as the central layer of a small Burgers vector screw dislocation – see Figure 26(a) and (b) in (*13*)). Therefore, a layer close to a minimal surface, and more generally a layer with negative Gaussian curvature, is expected to have a smaller curvature energy than a layer of the same area with $G > 0$, which favours type I FCDs. Another element to stabilise $G < 0$ is the *saddle-splay* modulus, whose sign is indifferently >0 or <0. Clearly, $\bar{K} > 0$ favours $\sigma_E\sigma_H < 0$. We refer the reader

to (*13*) for a description of the energetics of defects in a SmA; (*27*) is dedicated to the case of FCDs with negative Gaussian curvature, with a full account of the saddle-splay contribution.

2.2 Kinks and imperfect FCDs

When they are in contact, the interplay between a disclination conic and a dislocation shows up specific features that result in a local distortion of the conic away from its ideal elliptic or hyperbolic shape, at the location where the two defects meet. Such local distortions are called *kinks*. They have recently been reported in smectic phases of various LC materials (*28, 29*).

The concept of kink is very general; it is valid for all dislocation–disclination interactions, in smectics as well as in nematics and other media where the concepts of dislocation and disclination both make sense. The principle of the interaction is sketched in Figure 5.

Consider a disclination line, with rotation angle $\mathbf{\Omega} = \Omega\mathbf{t}$ about a fixed axis $\mathbf{t}$, made of two half infinite *wedge* segments[1], A′A and BB′, linked by a segment AB of *twist* character, a *kink* on the disclination A′B′ (Figure 5(a)). This geometry is equivalent to the geometry of Figure 5(b), where the segment BB′ has been 'smoothly' transported to the position BB″ and its orientation reversed, so that it can now be considered as carrying the rotation vector $-\mathbf{\Omega}$. The segments A′A and BB″ are wedge disclination segments of opposite rotations and carry together a translation

$$\mathbf{b} = 2\sin\frac{\Omega}{2}t \times \mathbf{AB}, \qquad (2)$$

where $\mathbf{\Omega} = \Omega\mathbf{t}$. Thereby they together are equivalent to a dislocation of Burgers vector $\mathbf{b}$ (*2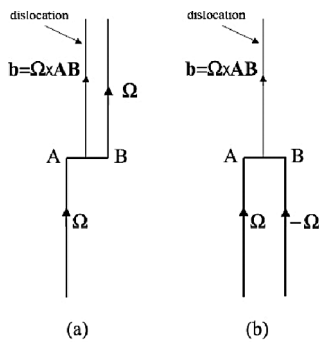6*). Thus, because of the law of conservation of the Burgers vector, a dislocation of Burgers vector $\mathbf{b}$ is attached to AB in Figure 5(b). Transporting BB″ back to BB′ 'smoothly', it appears that a dislocation with the same Burgers vector $\mathbf{b}$ is attached to the kink AB (Figure 5(a)). $\mathbf{b}$ has to be a translational symmetry of the medium under consideration, i.e. in a smectic a multiple of the layer thickness d_0, or a continuous translation parallel to a layer (which is a two-dimensional liquid media). However, this reasoning applies to any medium (see (*26*) for details), in particular for the role played by attached dislocations in the mobility and flexibility of disclinations, which we do not develop.

Let us apply Equation (2) to the FCD case. The Burgers vectors of the attached dislocations are either perpendicular to a direction belonging to the plane of the ellipse or of the hyperbola, if the kink is parallel to these planes (first type), or parallel to the plane of the ellipse or of the hyperbola, if the kink is orthogonal to these planes (second type). However, whichever the case may be, the Burgers vectors, which are along the translation symmetry directions, have to be either perpendicular to the smectic layers, if the broken translations are quantised ($b = nd_0$), or parallel to the layers if the broken translations are continuous. Again, observe that the foregoing considerations do not appeal at all to the topological theory of defects, but to the more ancient VP, suitably extended with the notion of kink (*26*). Figure 6 features an ellipse (very close to a circle) with

Figure 5. (a) Kink on a dislocation of strength $\mathbf{\Omega}$, $\mathbf{b}$ is the Burgers vector total attached to AB; (b) same as (a) with another orientation of a part of the line, exhibiting the equivalence of a dislocation and two disclinations of opposite signs at a distance AB.
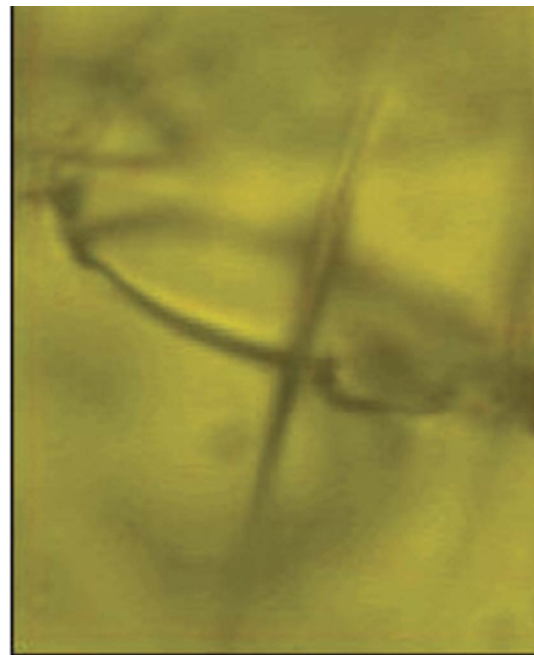

Figure 6. Macroscopic kink on an ellipse of small eccentricity. The dislocations attached to this kink have a Burgers vector orthogonal to the plane of the ellipse, and are located outside the FCD – see text (courtesy of Yu. A. Nastishin).

a macroscopic kink in the plane of the ellipse – according to Equation (2), the Burgers vector total of the attached dislocations is perpendicular to this plane. Since the Burgers vector is orthogonal to the layers, one expects that these dislocations pierce a set of layers quasi-parallel to the plane of the ellipse. Such layers are present outside the focal domains, which suggests that the attached dislocation lines are outside the FCD.

In Section 3 we discuss how the ellipse of a FCD can be understood as a kinked disclination, with a density of dislocations attached to it.

2.3   *The double helix*

The geometry of Figure 7(a) represents the *ideal* configuration for the central region of a screw dislocation with a giant Burgers vector; this configuration is ideal in the sense that it captures the main incentive for the recomposition of the screw dislocation singularity into a DH; namely, it guarantees the parallelism of the layers, at least in the region limited to the interior of the helices. However, it cannot be so outside, and the observed DHs are in fact much distorted compared to the ideal configuration, as we explain below.

In Figure 7(a) the central layer $H(0)$, which contains the axis of the screw dislocation, is a ruled helicoid of pitch $p = b$. The other layers, $H(i)$, are stacked upon $H(0)$ at distances id_0, $i = 0,1,2,\ldots$; all the $H(i)$s being parallel to $H(0)$ and parallel between themselves have common straight normals. The $H(i)$s, $i \neq 0$, are not minimal surfaces. Therefore, there is some curvature energy but no strain energy. Furthermore, there is no core singularity.

However, a singularity still exists, but it is rejected along the *focal surfaces* of the parallel $H(i)$s. These focal surfaces are two equal helicoids, with the same pitch as

the dislocation; each of them has a helical cuspidal edge, located at a distance $b/2\pi$ of the axis. Hence the name of *DH* for the cuspidal edges, which constitute two visible singularities (Figure 7(c)), as we now explain. Notice that the normals to the layers (which are horizontal in Figures 7(a) and 7(b)) join one helix point to another one on the other helix: the helices are conjugate. The region immediately beyond the cuspidal edge is covered twice by the layers – the helical geometry cannot be continued smoothly. Empirically, one observes that the SmA phase is arranged as in Figure 7(b), outside the cylindrical region defined by the helical cuspidal edges. The cuspidal edges then appear as *two disclinations* of rotation angle π, about which the helicoids are folded.

A DH is obviously very different to an imperfect FCD, because the conjugate focal surfaces are not degenerated to lines. Therefore, the imperfections cannot be analysed in low energy kinks. Williams, who first discovered DHs in the SmA phase of a nematogenic compound (*21*), has noticed how they originate as very distorted disclinations in a twisted nematic, at the N $\Rightarrow$ SmA transition. In the first stage of this process one observes fragments of conjugate ellipses and hyperbolae, which transform into fragments of helices.

A side remark: in the astonishing B7 phase, which is a chiral lamello-columnar phase, the inner part of the cylinder takes the ideal configuration of Figure 7(a), because it cannot smoothly be prolonged outside, the outer part is totally disorganised, i.e. is liquid (*30, 31*).

3.   **Grain boundaries**

3.1   *The $\omega = 0$ Apollonian packing*

This is de Gennes' main contribution to the subject of FCDs, and if we are not misled, his last effort in the physics of LCs *per se*, a domain of research that he did not encourage his former collaborators in this field to pursue. This was when he moved in 1972 from the Laboratoire de Physique des Solides in Orsay to the College de France, where his great accomplishments in the physics of polymers were to be completed. De Gennes was used to totally abandoning a former subject of research when he entered a new one, sometimes ostentatiously distancing himself from the first one, for example when he passed from superconductors to LCs. He realised how this attitude was excessive when high temperature superconductors were discovered. He was also used to marking the end of an effort in a given domain by the publication of a book that closed the case for a time. 'The Physics of Liquid Crystals', published in 1974 (*32*), was the bible of a generation of scientists. This text was little amended, but largely augmented 20 years later by Prost, with new topics such as columnar, incommensurate phases and phase transitions.
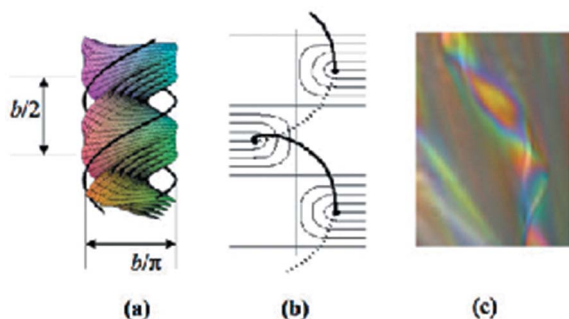

Figure 7. (a) Three-dimensional perspective view: stacking of helicoidal layers on each side of central ruled helicoids and of the two disclinations about which they are folded. Only the central region inside the cylinder limited by the disclinations is drawn; (b) schematical representation of a cut along a meridian plane; (c) a DH in the SmA phase of cholesterylnonanoate, with $b \approx 50\,\mu$m (courtesy of C. Meyer). Adapted from (*13*) for (a) and (b).

Bidaux *et al.* (*10*) recognised that the very reason for the FCDs to occur in lamellar systems is the necessity of satisfying boundary conditions that often do not allow the system to adopt the geometry of flat parallel layers. As a particular example, Bidaux *et al.* (*10*) imagined a grain boundary, as in Figure 8, that serves to match the conflicting boundary conditions at the two parallel plates confining the smectic material: one plate sets a perpendicular orientation of the LC molecules and another sets a tangential orientation. They proposed that the grain boundaries are relaxed by TFCDs (*10*).

In fact, the grain boundary shown in Figure 8 cannot be relaxed by TFCDs with bases of zero eccentricity; as explained later, it can be related by FCDs of non-zero eccentricity. The TFCD (as opposed to a regular ellipse-hyperbola FCD) geometry implies that the layers on both sides of the grain boundary are in fact parallel to each other rather than tilted by 90 degrees as in Figure 8. In other words, the TFCD grain boundary is of vanishing misorientation $\omega = 0$ and there is no physical reason to introduce the TFCD with curved layers in the situation when the SmA can be perfectly uniform. Although the TFCD approach does not reflect the physical essence of the grain boundary problem, it does allow one to trace the important geometrical features of filling the space with FCDs, namely, (a) the scaling character of filling the plane with the bases of FCD and (b) the nature of the residual areas between the FCD.

The iterative filling of the grain boundary with the circular bases of the TFCD considered in (*10*) was based on the well-known Apollonius' packing of circles, in which one starts with a system of large touching circles and then fills the interstices between them with
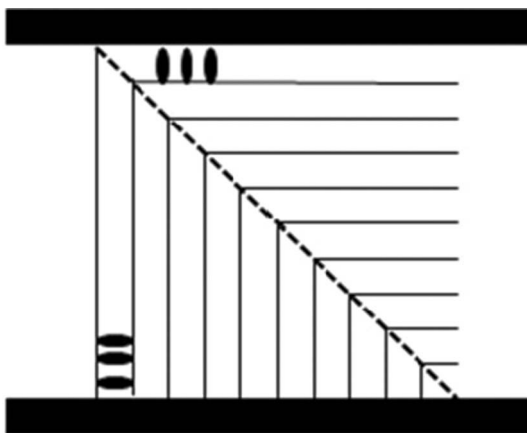

Figure 8. An example of the hybrid boundary conditions imposed on the SmA sample by a pair of flat bounding plates. The boundary conditions are relaxed by the grain boundary. As explained in the text, the geometrically correct relaxation of the grain boundary in this figure should contain ellipses of non-zero eccentricity, in this particular case of $e = 1/\sqrt{2}$.
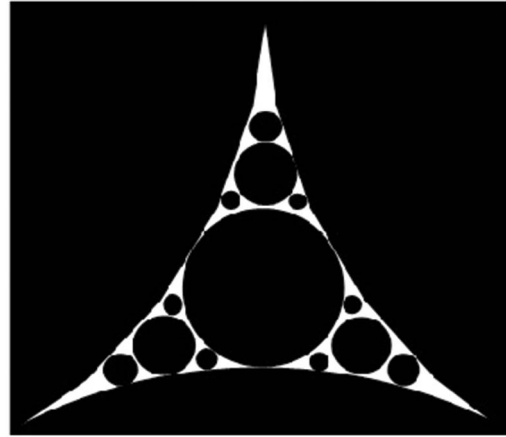

Figure 9. Apollonius' packing of circles.

smaller circles that are tangent to those already present and then repeats this iteration process (Figure 9). If L is the radius of the largest circles and b of the smallest, one expects that all the relevant quantities, such as the number g of circles of radii between L and b, their perimeter P and the residual area left not covered by the circles Σ, scale algebraically with the dimensionless quantity L/b (*10*):

$$g(b) = const.\left(\frac{L}{b}\right)^n; P(b) = const.b\left(\frac{L}{b}\right)^n;$$
$$\Sigma(b) = const.b^2\left(\frac{L}{b}\right)^n. \tag{3}$$

Relatively recent numerical calculations (*33*) show that the exponent n is approximately 1.3057. Interestingly, Bidaux *et al.*, using computer simulations available to them in the early 1970s, found a very close value of $n \approx 1.3069$. In the late 1970s, Mandelbrot presented the model of (*10*) as one of the first clearly recognised examples of fractal behaviour in physical systems (*34*). He commented that 'if it were possible to proceed without end, we would achieve exact Apollonian packing'.

Of course, one cannot proceed without end. Physically, the iterations should stop when the size of the TFCD become so small that the associated strong curvatures of layers are no longer compatible with the very structure of the SmA phase. The energy and the radius of the smallest domain of grain boundary with a zero tilt have been estimated in (*10*) as follows.

The energy of a TFCD of radius b scales as Kb, hence the contribution to the total energy of the circles of radius $R > b$ scales as $W_{line} \sim KP(b) = const.Kb(L/b)^n$. The residual regions are elastically deformed over a distance from the plane of the boundary of order $\lambda = \sqrt{K/B}$, hence $W_{resid} \sim B\lambda\Sigma(b) = const.B b^2 \lambda(L/b)^n$. After

minimisation of $W_{line} + W_{resid}$ with respect to b, the value of b at the final iteration is $b^* \sim \sqrt{K/B} = \lambda$, i.e. a microscopic length determined by a ratio of the curvature and compressibility elastic moduli. This result comes as no surprise, since the grain boundary is located in the SmA bulk, and the only characteristic length scale of the SmA bulk is the smectic layer thickness d_0, or the closely related penetration length $\lambda = \sqrt{K/B} \approx d_0$. The energy per unit area of the grain boundary is $\sigma_{FCD} \sim L^{-2}(L/b^*)^n B\lambda^2 b^*$.

As suggested by Bidaux *et al.* (*10*), the closest physical realisation of the TFCD model might be a SmA in a 'hybrid' aligned cell (Figure 8). For example, it might be a film of SmA placed onto a surface of a fluid that does not mix with the SmA material and sets tangential orientation of the molecules. A suitable pair for fluid-SmA is glycerine and octylcyanobiphenyl (8CB). At the upper surface, left free, the orientation of 8CB molecules is perpendicular. The texture of such a hybrid aligned SmA film reveals that the TFCDs do indeed form an iterative pattern of Apollonius' type.

However, the experimental pattern (Figure 10) differs from the original model in two aspects. Firstly, the circular bases of the TFCDs are located at the SmA–glycerine interface and not in the bulk of the LC. Secondly, the iterations stop at scales much larger than the molecular one. These two features are in fact deeply related, as the pattern is determined by the balance of surface anchoring energy and elastic energy (*35, 36*). By placing the circular base of a TFCD at the interface with glycerine, one decreases the total energy of the system by the surface anchoring energy gain $\sim \pi b^2(\sigma_\| - \sigma_\perp) < 0$; here $\sigma_\|$ and $\sigma_\perp$ are the surface energy densities for molecules oriented parallel and perpendicular to the substrate, respectively, $\sigma_\| < \sigma_\perp$. Balancing this with the elastic energy of curved layers Kb, one finds the minimum size of the TFCD as $b^* \sim \frac{K}{\sigma_\perp - \sigma_\|}$ (*35*), which is of the order of 1–10 mm, for the typical estimates $K \sim 10$ pN, $\sigma_\perp - \sigma_\| \sim 10^{-5}$ J m^{-2}. The latter estimation can be modified by taking into account the additional surface tension term associated with the depression of the free surface near the axis of the TFCD (*37*), but the important feature to observe is that it is the tangential surface anchoring and rectangular confining geometry that drive the formation of TFCDs of size $b \geq b^*$.

3.2   *The disclination ellipse as a kinked disclination*

Applying Equation (2) to a circular wedge disclination (the circle in a TFCD), with $AB = d\mathbf{s}$ the vector distance between two infinitesimally close points on the circle, yields $\mathbf{b} = 0$. For a disclination ellipse (Figure 11) the local rotation vector belongs to the plane of the ellipse and is along the intersection of the layers with the plane of the ellipse, inside the ellipse (*28*). The
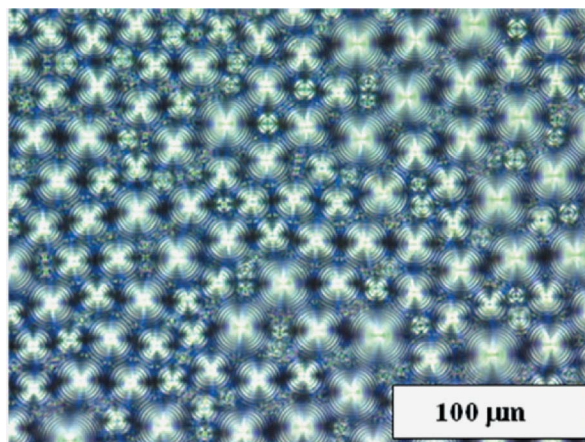
(a)
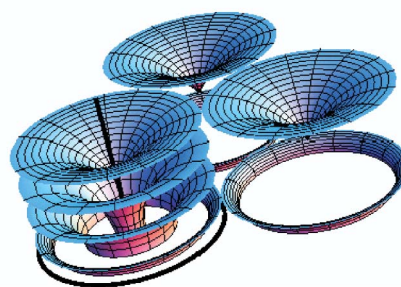
(b)

Figure 10. An iterative filling of the SmA film (octylcyanobiphenyl) with TFCDs seen through a polarising microscope as bright discs with Maltese crosses. (a) The film is placed on the surface of glycerine that produces degenerate tangential anchoring of SmA molecules at the lower boundary; at the upper free boundary, the orientation of molecules is perpendicular. The iterative system of TFCDs interrupts at the scale of a few micrometers. The scheme in (b) shows three families of Dupin cyclides corresponding to three touching TFCDs. The circular and axial defect lines are shown only for one TFCD. For the two others, only some of the Dupin cyclides are shown. The circular defects lie in the plane of the interface. Only one iteration of TFCDs is shown. The interstices can be smoothly filled with layers parallel to the interface with the substrate. Note that the smectic layers approach the interface under the right angle.

Burgers vector of the dislocation attached to a segment of the ellipse between r and $r + dr$ (Figure 11) is

$$d\mathbf{b} = 2 \sin\frac{\pi}{2}\mathbf{t} \times \mathbf{MN} = 2dr\ \mathbf{u}, \qquad (4)$$

where $\mathbf{u}$ is a unit vector orthogonal to the plane of the ellipse. Hence, the total Burgers vector attached to a disclination ellipse is $\int d\mathbf{b}$ integrated along the ellipse between the two apices, namely $\mathbf{b} = 2\ c\ \mathbf{u}$. It is useful to let the length of the long axis of the ellipse appear, so that we have $\mathbf{b} = 2\ a\ e\ \mathbf{u}$. The eccentricity e can be
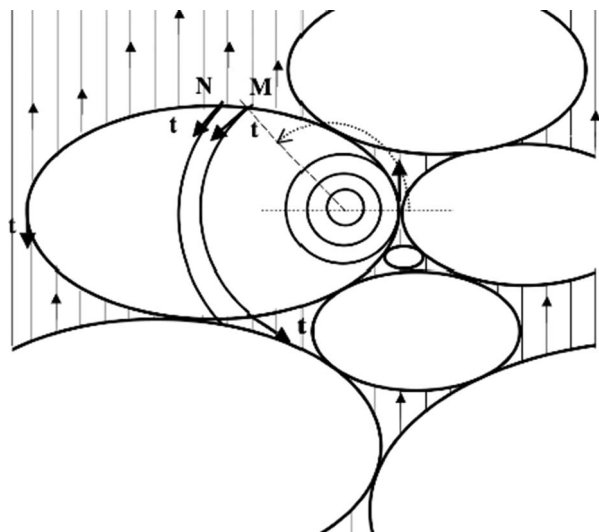
Figure 11. Ellipses of the same eccentricity tiling a portion of a grain boundary. The radius of curvature of the circle of the marked ellipse, centred in the focus F and tangent to the apex, is *a–c*, which is smaller than the radius of curvature of the ellipse at the apex. This circle is thus entirely inside the ellipse. All the circles and the arcs of circles of the figure are centred in F. They figure the intersections of the smectic layers with the plane of the ellipse. t is the direction of the local rotation vector of the disclination. The dislocation segments that run from an ellipse to another one have all the same orientation and the same density $b/2a = e$.

expressed in function of the angle $\omega/2$ of the asymptotes of the hyperbola with **u**, $e = \sin\omega/2$, so that

$$\mathrm{b} = 2\, a \sin\frac{\omega}{2}\, \mathrm{u}. \qquad (5)$$

Thus, a disclination ellipse is a kinked disclination whose local rotation vector is $(\pi/2)\mathbf{t}$. The plane of the ellipse separates two smectic domains, which, inside the same FCD (at a distance along the asymptotes), are misoriented *one* with respect to the other by an angle of $\omega \neq 0$ about a rotation axis along the minor axis of the ellipse (see Figure 3(a)). This explains why *tilt* grain boundaries can be made of a planar packing of ellipses of the same eccentricity and whose minor (and thus major) axes are parallel.

3.3   The ω ≠ 0 Apollonian packing

There is a complete mapping between the $\omega = 0$ Apollonian packing and the $\omega \neq 0$ packing just mentioned – each circle of the Apollonian packing is replaced by an ellipse of eccentricity $e = \sin\omega/2$. The ellipses having parallel major and minor axes, all the asymptotic directions of the related hyperbolae are parallel. Each FCD of the $\omega \neq 0$ tilt boundary is complete (as sketched in Figure 3(a)) and is in contact with
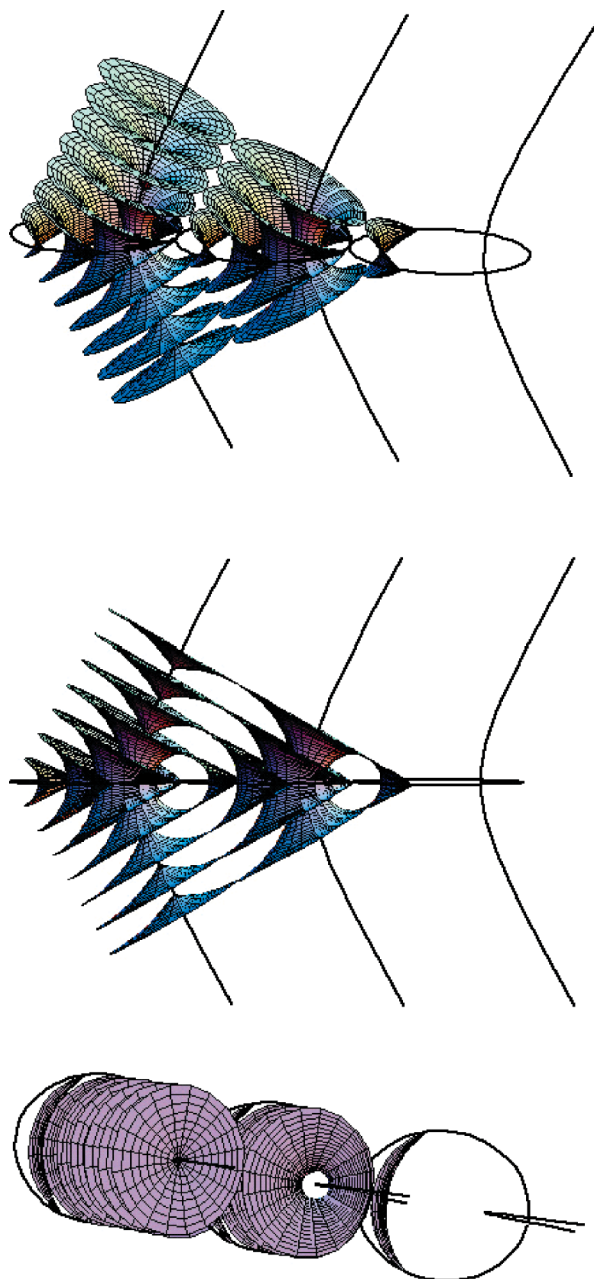
Figure 12. Perspective view of FCDs of the same eccentricity in contact in a grain boundary.

a neighbouring complete FCD along two generatrices symmetrical with respect to the plane of the ellipse (Figure 12) – it is in a one-to-one relationship with a complete toric domain belonging to the $\omega = 0$ Apollonian tiling. One can therefore speak of '$\omega \neq 0$ *Apollonian packing*', which has the same fractal properties as the $\omega = 0$ Apollonian packing. We shall not dwell any longer on this geometry, and we refer the reader to (22) for a complete discussion. However, the energy properties, which can be calculated in the same

fractal approach as for the $\omega = 0$ case, depend on the angle of misorientation ω, so that the residual areas might be, according to the case, large or microscopic, and the limiting scales of the fractal distribution thus different from the $\omega = 0$ Apollonian packing.

The residual regions are pieces of grain boundaries and adopt either a model of a curvature wall or of a dislocation wall (also called the Grandjean model), which we discuss hereunder. The calculation of the energy of the grain boundary shows that the Grandjean model is favoured for small misorientations (when the layers are practically parallel to the grain boundary) and the curvature model is favoured for large ones (when the layers are closer to the normal than to the grain boundary) (*22*) (Figure 13).

3.3.1   *The Grandjean model*

Again, the dislocations that are attached to the ellipse of an isolated FCD, characterised by the quantities *a* and *e*, have a total Burgers vector $b = 2$ *ae*. In practice, the dislocations run parallel to the tilt axis, all with the same sign and a constant density $b/2a = e$ (Figure 11). Since $e = \sin\omega/2$ the misorientation of the related grain boundary is precisely ω; the layers in the regions inside the FCDs and outside are in register. In a TFCD, the circle is of vanishing eccentricity, $b = 2a\ e = 0$ – there are no dislocations attached to it. A TFCD can be smoothly embedded into a system of flat and parallel layers with $\omega = 0$. Experimental realisations of ellipses and their attached dislocations have been observed in light microscopy, in both thermotropic (*38*) and lyotropic (*39*) SmAs. It is directly visible that the dislocations have large, giant Burgers vectors, whose magnitude scales with the size of the ellipses, and that they are located in the plane of the ellipses. The dislocation lines have an edge character. This is in contrast with the result obtained for $\omega = 0$ (Section 3.2), which predicts residual regions of microscopic size.
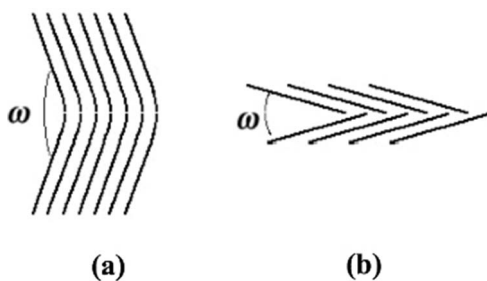

Figure 13 (a) Curvature wall; (b) Grandjean wall. In both cases, the lines represent the layers. Adapted from (*13*).

3.3.2   *The curvature model*

At large misorientations, the residual areas are relaxed by curvature walls. The energy cost has two origins: the curvature walls in the residual regions (but the layers do not abut abruptly on the grain boundary), and a mismatch in curvature of the layers inside and the layers outside the FCDs. The curvature wall energy (per unit area) can be written as (*39*)

$$F_{curv} = 2B\lambda\left(\tan\frac{\theta}{2} - \frac{\theta}{2}\right)\cos\frac{\theta}{2}, \theta = \pi - \omega. \quad (6)$$

Two remarks:

(i)   An implicit assumption of the model is the existence of an Apollonian tiling, i.e. a compact packing with tiles of different sizes, not fixed in advance, and with no entropy of mixing, since an iterative filling obeys quasi deterministic rules (see (*40*) for a comparison between scaled and entropic tilings). The smaller conics are certainly those that would contribute more to the entropy, but such objects are not present, because the residual areas are macroscopic. This remark might be a strong indication of the physical reality of the Apollonian tiling.

(ii) The model above has been discussed for a SmA. However, its basic features remain valid for other lamellar phases, e.g. SmC LCs, in which *chevron* walls are often split into FCDs (*41*). The chevron formation is ruled by surface anchoring and depends on the actual geometry. The tilt of molecules within the SmC layers causes other complications, both topological (disclination lines in the vector field of molecular projections onto the layers (*42–44*)) and energetical (a finite energy of tilt).

4.   Boundary conditions and colloidal templating

The surface anchoring driven process of TFCD formation is in fact very widely met. The best known example dates back to the pioneering work of Friedel (*5*) and the formation of a SmA phase upon cooling from the isotropic melt that occurs through nuclei of complex shape and structure (Figure 1(b)) called the 'bâtonnets' by Friedel. The simplest model of a bâtonnet would be a sphere with tangential boundary conditions. Note that these boundary conditions are incompatible with the concentric packing of the SmA layers, which would otherwise be one of the candidates for the local arrangement of the layers in a spherical volume. However, the equilibrium can be achieved by a *combination* of layers with spherical curvature and TFCDs. In 1982, Sethna and Kleman demonstrated (*45*) that a family of conically shaped FCDs with a common apex can have the
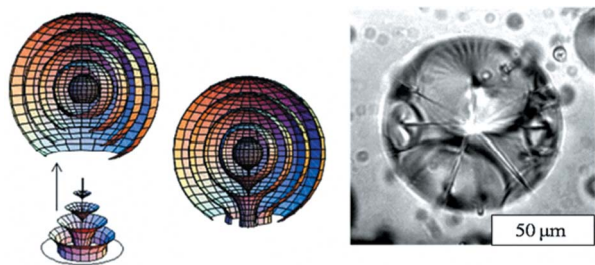
Figure 14. Smooth matching of spherical layers and layers belonging to TFCDs of conical shape. Texture of a SmA droplet suspended in the glycerine matrix with the family of TFCDs and interstices filled with spherical layers, according to (*34*).

interstices between them filled with spherical layers that have the centre of curvature at the common apex. Figure 14 illustrates the smooth matching between a conically shaped TFCD and a spherical packing. Note that the layers approach the conical boundary separating the two types of packing at a right angle, thus there is no surface discontinuity there. The iterative filling starts at the scales of the radius of the sphere and ends at the scales $b^* \sim K/(\sigma_\perp - \sigma_\parallel)$ (*35*). Fournier and Durand (*46*) have extended this analysis to the general case of non-spherical bâtonnets, thus taking into account another important energy contributed, associated with the surface tension of the SmA–isotropic interface.

The interest in the substrate-induced formation of TFCDs has recently been revived thanks to the observation that they can be formed in a well-controlled geometry of confinement, either at substrates with patterned anchoring conditions (*47, 48*) or in rectangular microchannels (*49–52*). By controlling the surface properties and the type of SmA material, one can control the smallest size of the domains, b^*. On the other hand, the largest size L can be controlled by the thickness of the SmA slab, or by the depth of the channel in which the SmA is confined. Of course, for very narrow channels, not only the depth but also the width of the channel can be used as a controlling parameter (*52*). In some applications, it is desirable to overcome the effect of hybrid alignment and to achieve a uniform alignment of layers. This can be done by reducing the thickness of the SmA film below some critical value related to b^*. Recently, Reznikov *et al.* (*53*) demonstrated that the FCDs can be suppressed if the SmA phase forms from the isotropic phase slowly and in the presence of a strong temperature gradient. Note that the dynamical aspects of FCDs are still poorly understood. FCDs can also be introduced in the SmA samples by external electric and magnetic fields (*54–60*), even if the boundary conditions favour a uniform system of layers. Some of the first electrically-driven display modes using LCs

were based on focal conic textures in smectic materials (*32*). Nowadays, electrically driven formation of focal conic textures in cholesteric LCs is one of the most promising directions in the development of bistable displays and displays on flexible substrates that use no polarisers, see, for example, (*58*). From a theoretical point of view (*59, 60*), field-induced nucleation is practically impossible without artificial sites of nucleation, such as foreign particles, dislocations, small 'seed' FCDs, etc, as the process is determined by the balance of the elastic energy that is linear in the FCD size, $\sim Kb$, and the dielectric or diamagnetic anisotropy energy proportional to the volume of the distorted region, $\sim b^3$. The balance of the two terms produces a huge energy barrier (*59, 60*) that cannot be overcome in homogeneous nucleation.

The surface-induced regular arrays of TFCDs can be used as templates to create similar arrays of colloidal particles (*51*). Experimentally, it was observed by Yoon *et al.* (*51*) that small colloidal spheres added to the SmA material end up distributed regularly in the TFCD hexagonal array (Figure 15). To explain this phenomenon, we recall that the behaviour of a colloidal particle in the LC environment is strongly dependent on the surface anchoring at the particle–LC interface and the elasticity of the LC host (*61*). In particular, small particles tend to migrate towards linear defects, such as disclinations, thus reducing the overall energy of the system (*62*). In our case, such a line is the vertical line defect. Another line defect is the circular base of the TFCD, but the particles did not accumulate there, despite the fact that gravity would have favoured this location as opposed to the location in the bulk of the film. A plausible reason for the particle's 'levitation' in the bulk might be the tangential surface anchoring of SmA molecules at its surface, similar to that described by Blanc and Kleman (*63*).
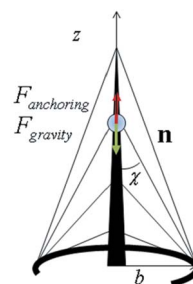

Figure 15. Colloidal templating with TFCDs. The array of TFCDs in a microchannel filled with a SmA is used to arrange 1 mm colloidal particles into regular hexagonal arrays (*50*). The particles are trapped at the axial defects of the TFCDs and can levitate in the bulk resisting the gravity effects.

Let us consider the difference in the molecular structure at the core of the vertical and circular defects (Figure 15). Locally, the director $\hat{\mathbf{n}}$ around the circular defect is pointed normally to the defect core, forming a radial structure. At the vertical line defect, the situation is different: $\hat{\mathbf{n}}$ forms a cone with an angle at the apex $\chi = \arctan \frac{b}{z}$ (measured with respect to the z-axis) that decreases from $\chi = \pi/2$ at the lower end of the defect, $z = 0$, to a smaller value as the z-coordinate increases. The surface anchoring energy cost of placing the particle at different z locations along the axis can be estimated by integrating the standard Rapini–Papoular anchoring potential (24) over the spherical surface of the particle, $F_{anch} = (\sigma_\perp - \sigma) \oint \left[1 - (\hat{\mathbf{n}} \cdot \hat{\mathbf{v}})^2 \right] ds$, where $\hat{\mathbf{v}}$ is normal to the particle's surface. We assume that the particle radius r is much smaller than the radius b of the TFCD, so that variations of χ at the particle's surface are neglected. A routine integration yields

$$F_{anch} = \frac{4}{3}\pi r^2 (\sigma_\perp - \sigma_{||}) \left(1 + \frac{1}{1+\delta^2} \right), \qquad (7)$$

where $\delta = z/b$; in other words, the larger the value of z, the smaller the anchoring penalty for having the particle at the core of the defect. Note that the last formula is applicable for any location at the circular defect, in which case $\delta = 0$, and the anchoring energy assumes its maximum value. As for the axial line defect, the vertically-resolved force corresponding to the potential (8) and pushing the particle upwards, $f_{anch} = -\frac{\partial F_{anch}}{\partial z} = \frac{8}{3}\pi r^2 \frac{\delta}{b(1+\delta^2)^2}(\sigma_\perp - \sigma_{||})$, is significant. For the typical (35) $(\sigma_\perp - \sigma_{||}) \approx 10^{-5}$ Jm^{-2}, $r = 0.5\,\mu$m, $b = 2\,\mu$m, and $\delta \sim 1$, one finds $f_{anch} \approx 10$pN, much larger than the gravity force $f_g = \frac{4}{3}\pi r^3 \rho g \sim 0.01$ pN (here $\rho \sim 10^3$ kg m^{-3} is the difference in the densities of silica particle and a LC, $g = 9.8$ ms^{-2} is the standard gravity).

5.   Focal conic domains and three-dimensional imaging

The studies of relatively complex geometries of distortions associated with FCDs and other configurations inspired an interest in the development of new approaches to three-dimensional LC images. A regular polarising microscopy texture, such as the one in Figure 1, is produced after the polarised light travels through the birefringent specimen; the modulation in light intensity is determined by the optical retardance integrated over the entire pathway of light. Therefore, polarising microscopy yields only a two-dimensional image of the three-dimensional configuration. Note that in a regular uniaxial SmA, the local optic axis coincides with the normal to the layers. The director profile along the direction of observation ('vertical cross section') is hard to

decipher; as illustrated by Bellare *et al.* (64), polarising microscopy images of such different objects as spheres and FCDs in flat samples of SmA are practically indistinguishable. Of course, a sample can be constructed in such a way that it can be viewed from different sides (a cylindrical capillary, for example), but this solution is not a universal one, as in most cases researchers are interested in sandwich-like samples with a thin (tens of microns or less) LC slabs. It is precisely the director configuration in the vertical cross-section of such a cell that is often the most valuable and desirable in studies of LCs.

Three-dimensional imaging of LCs can be achieved relatively easily with Fluorescence Confocal Polarising Microscopy (FCPM) (65, 66), confocal Raman microscopy (67) and, with a significantly more complicated approach, by coherent anti-Stokes Raman scattering (CARS) microscopy (68–70). In FCPM, the LC is doped with a fluorescent dye, the molecules of which are sufficiently anisometric to align themselves parallel to the LC molecules and thus parallel to the local director (we restrict the consideration by the simplest case of rod-like molecules) (65, 66). If the sample is probed with a tightly focused and linearly polarised laser beam, this will cause fluorescence of the dye. The intensity of fluorescence would depend on the angle α between the polarisation of light and the transition dipole of the dye, typically $I \propto \cos^4 \alpha$. The confocal scheme of the microscopy allows one to register the fluorescent signal only from the preselected small volume in which the beam is focused. Light coming from the neighbourhood of the inspected 'voxel' is blocked from reaching the detector. To obtain a three-dimensional image of the whole sample, the tightly focused laser beam scans the specimen voxel by voxel. Using a computer, the data, which essentially describes a three-dimensional pattern, can be presented as horizontal or vertical cross-sections of the sample. Of course, the confocal scheme is intrinsically at odds with the birefringent nature of the inspected medium, as the ordinary and extraordinary waves cannot be focused in the same way. However, the difference in the location of the focus of the two modes is determined roughly as $\delta \sim z(n_e - n_o)/\bar{n}$, where z is the depth of scanning in the birefringent medium and n_e, n_o, $\bar{n}$ are the extraordinary, ordinary and some average refractive indices of the LC. Therefore, even for relatively highly birefringent materials with $(n_e - n_o)/\bar{n} \sim 0.1$, one can still achieve a resolution on the order of 1 μm with samples of 10 μm thickness. Of course, better results are achieved for low birefringent LCs. Figure 16 shows the image of a FCD with a base located at the boundary of the SmA cell.
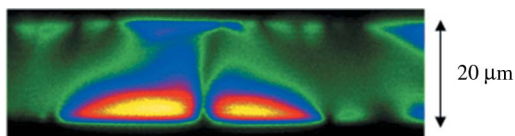
Figure 16. FCPM texture of the vertical cross-section of a SmA cell with a FCD with the base at the bottom plate. The dark bands at the top and bottom are the two glass plates bounding the slab. The texture is provided by I. Smalyukh.

FCPM allows one to use more than one fluorescent dye in order to trace the different directions of the molecular order. This approach allows one to explore FCDs in biaxial SmAs (66), in which the one-dimensional positional order is accompanied by a nematic-like order within each layer with the director $\hat{\mathbf{n}}_b = -\hat{\mathbf{n}}_b$, which is perpendicular to the normal $\hat{\mathbf{n}}_a = -\hat{\mathbf{n}}_a$ to the layers. It turned out that the FCDs in these phases can be associated with linear disclinations in the $\hat{\mathbf{n}}_b$ field and the distortions extend well beyond the base of the FCDs (66).

Although the amount of dye needed to achieve a good quality imaging with FCPM is very small, only about 0.01 wt% as compared to the amount of the LC itself, the very presence of the dye is not a desirable feature. Recently, the possibilities of using a label-free approach for three-dimensional imaging of LCs have been demonstrated. The techniques are based on confocal Raman microscopy (67) and on less invasive and faster CARS microscopy reviewed recently by Evans and Xie (68). Not only are CARS and Raman microscopies label-free; they also allow one to determine the three-dimensional pattern of orientation of preselected chemical bonds in the sample, such as the CN, CH, or CO bond. In the CARS process, the sample is excited by two laser beams, at two optical frequencies, ω_p ('pump') and ω_s ('Stokes'), one of which is tuneable so that the beating frequency (the difference $\omega_p - \omega_s$) can be adjusted to be in resonance with a preselected molecular vibration in the sample. If such a resonance is achieved, the sample generates a strong signal at the anti-Stokes frequency, $\omega_{as} = 2\omega_p - \omega_s$, through a four wave mixing process. This signal produces the optical contrast in imaging; its intensity depends on the polarisation of all the light beams involved and on the state of orientation of the molecular vibration. The advantage of CARS over Raman microscopy is mostly in the much faster acquisition of the image (69). Of course, CARS imaging of LCs suffers from the same limitations related to birefringence as FCPM does, as discussed in (69, 70). However, a huge advantage of CARS is in the opportunity to obtain, in a non-invasive way, the chemically sensitive information on three-dimensional patterns of orientational order.

6. Conclusion

The considerations above have been restricted to the simplest lamellar phase, the uniaxial smectic A phase. However, FCDs appear as a general feature in other lamellar phases, whenever a one-dimensional positional order and layered structure is accompanied by a fluid- or nematic-like two-dimensional order, such as SmC, biaxial SmA, and even cholesteric phases, provided the scale of distortions is much larger than the cholesteric pitch. As already indicated, FCDs in these phases are accompanied by additional defects in the vector (or director) field specified by the molecular order within the layers. FCDs are often seen in SmC phases decorating the so-called 'chevron' structures (41, 71); the latter represents a domain wall that forms when the smectic layers, being originally perpendicular to the bounding plates, shrink and tilt. The overall geometry is similar to the tilt grain boundary that is relaxed either through the FCDs, as considered above for the SmA phase, or through a wave on undulations near the chevron ridge (72).

An especially intriguing question is whether the FCDs can appear as 'intrinsic' structural elements that guarantee the stability of phases in which the layers are bent rather than flat. A good example is the sequence of the sponge phase-lamellar phase-micellar phase observed in the lyotropic phases of certain surfactants. The lamellar phase, the ground state of which is flat layers, exhibits FCDs of different Gaussian curvature when the system approaches the transition into a different phase. In the vicinity of the micellar phase, one observes the FCD-II of positive Gaussian curvature (12), while in the vicinity of the sponge phase, one observes the FCD-I of negative Gaussian curvature and saddle-splay type layer deformations (20, 40). Metastable 'onion'-like structures have been also observed as the nuclei of lamellar phase by Iwashita and Tanaka (73). In principle, the two phases neighbouring the lamellar phase can be considered as assemblies of elementary FCDs, of either type I or type II. One can certainly learn about the corresponding phase transitions by considering elementary excitations in the form of FCD-I and FCD-II. DiDonna and Kamien (74) proposed a smectic 'blue phase', a thermotropic analogue of the 'sponge phase', in which the layers added on top of a seed layer represent a minimal surface. As compared to the system of flat layers, such a configuration is stabilised by the gain in energy of saddle-splay deformations. Note that a set of FCDs can also provide a gain in saddle-splay energy; moreover, Dupin cyclides, being strictly parallel to each other and having focal lines rather than focal surfaces, might yield an additional energetic advantage as compared to the structure based on the minimum surface.

The role of dislocations in the properties of smectics (*75, 76*) under flow has recently emerged as a new subject of research. It is well known that dislocations are the leading actors in the plastic deformation of solids (*23*), and it is therefore of a particular interest to estimate in which respect smectics can flow like solids (*77*). It appears that screw dislocations (orthogonal to the layers) and edge dislocations (parallel to the layers) have different rheological behaviours (*75–77*), but a number of questions remain to be explored, e.g. how dislocations affect the relation between the stress and the strain rate. On the other hand, practically nothing is known about the rheological properties of FCDs, although it is expected that the interplay with dislocations through the presence of kinks plays a leading role; in that respect, it is worth mentioning the observed changes of size and eccentricity of FCDs at the SmA–Nem transition (*28, 29*).

To conclude, the story of FCDs, started 100 years ago, continues to develop. One might expect the development of new refined display devices that use the light scattering abilities of FCDs in various electrically, thermally or optically driven media. FCD 'lithographic' templating is an entirely new and interesting direction. Even in the field of basic physics, the appearance of FCDs to guarantee the stability of various structures is still the phenomenon to explore. Finally, one might expect an entirely new level of excitement once the research shifts from the study of static problems to the dynamics associated with FCDs.

Note

[1]We recall that a *wedge* disclination line segment is a line segment parallel to the rotation vector, here denoted by $\boldsymbol{\Omega}$; a *twist* disclination line segment is perpendicular to the rotation vector $\boldsymbol{\Omega}$ (cf. (*23*)).

Acknowledgements

References

(1) Lehmann, O. *Die scheinbar lebenden Kristalle*; Eshlingen, 1907.
(2) Lehmann, O. *Die Lehre von den flüssigen Krystallen und ihre Beziehung zu den Problemen der Biologie*; Wiesbaden: Bergmann, 1918.
(3) Friedel, G.; Grandjean, F. *Bull. Soc. Fr. Minéral.* **1910**, *33*, 409–465.
(4) Hilbert, D.; Cohn-Vossen, S. *Geometry and the Imagination*; Chelsea Pub Cy: New York, 1952.
(5) Friedel, G. *Ann. de phys.* **1922**, *18*, 273–315.
(6) Bragg, W. *Nature* **1934**, *133*, 445–465.
(7) Chystiakov, I.G. *Sov. Phys. Usp.* **1967**, *9*, 551–580.
(8) Bouligand, Y. *Dislocations in Solids*; Elsevier: Amsterdam, 1980; Vol. 5, p. 299–347.
(9) Sluckin, T.J.; Dunmur, D.A.; Stegemeyer, H. *Crystals that flow. Classic papers from the history of liquid crystals*; Taylor & Francis: London/New York, 2004.
(10) Bidaux, R.; Boccara, N.; Sarma, G.; de Sèze, L.; de Gennes, P.-G.; Parodi, O. *J. Physique* **1973**, *34*, 661–672.
(11) Blanc, C.; Kleman, M. *Phys. Rev.* **2000**, *E62*, 6739–6748.
(12) Boltenhagen, P.; Lavrentovich, O.D.; Kleman, M. *Phys. Rev.* **1992**, *A46*, 1743–1746.
(13) Kleman, M.; Lavrentovich, O.D.; Nastishin, Yu. A. *Dislocations in Solids*; Elsevier: Amsterdam, 2004; Vol. 12, p. 147–271.
(14) Stewart, I.W. *Liquid Crystals* **1993**, *15*, 859–869.
(15) Fournier, J.-B. *Phys. Rev.* **1994**, *E50*, 2868–2871.
(16) de Gennes, P.-G. *C. R. Hebd. Séan. Acad. Sci.* **1972**, *275B*, 549.
(17) Brenner, E.A.; Marchenko, V.I. *Phys. Rev.* **1999**, *E59*, R4752–4753.
(18) Santangelo, C.D.; Kamien, R.D. *Phys. Rev. Lett.* **2003**, *91*, 045506-1–045506-4.
(19) Ishikawa, T.; Lavrentovich, O.D. *Phys. Rev.* **2000**, *E60*, R5037–R5037.
(20) Boltenhagen, P.; Lavrentovich, O.D.; Kleman, M.J. *Phys. II* **1991**, *1*, 1233–152.
(21) Williams, C.E. *Philos. Mag.* **1975**, *32*, 313.
(22) Kleman, M.; Lavrentovich, O.D. *Eur. Phys. J.* **2000**, *E2*, 47–57.
(23) Friedel, J. *Dislocations*; Pergamon Press: London, 1964.
(24) Kleman, M.; Lavrentovich, O.D. *Soft Matter Physics: An Introduction*; Springer: NY, 2003.
(25) Frank, F.C. *Disc. Far. Soc.* **1958**, *25*, 19–28.
(26) Kleman, M.; Friedel, J. *Rev. Mod. Phys.* **2008**, *80*, 61–115.
(27) Kleman, M.; Lavrentovich, O.D. *Phys. Rev.* **2000**, *E61*, 1574–1578.
(28) Kleman, M.; Meyer, C.; Nastishin, Yu. A. *Philos. Mag.* **2006**, *86*, 4439–4458.
(29) Nastishin, Yu.A.; Meyer, C.; Kleman, M. *Liq. Cryst.* **2008**, *35*, 609–624.
(30) Nastishin, Yu.A.; Achard, M.F.; Nguyen, H.-T.; Kleman, M. *Eur. Phys. J.* **2003**, *E12*, 581–591.
(31) Achard, M.F.; Kleman, M.; Nastishin, Yu.A.; Nguyen, H.-T. *Eur. Phys. J.* **2005**, *E16*, 37–47.
(32) de Gennes, P.G. *The Physics of Liquid Crystals*; Oxford, 1974; de Gennes, P.G.; Prost, J. *The Physics of Liquid Crystals*; 2nd edition, Oxford University Press: Oxford, 1994.
(33) Thomas, P.B.; Dhar, D.J. *Phys. A: Math. Gen.* **1994**, *27*, 2257–2268.
(34) Mandelbrot, B., 1983, The Fractal geometry of Nature, W.H. Freeman and Company, NY.
(35) Lavrentovich, O.D. *Zhurn. Eksp. Teor. Fiz.* **1986**, *91*, 1666; (*Sov. Phys. JETP* **1986**, *64*, 984–990).
(36) Lavrentovich, O.D. *Mol. Cryst. Liq. Cryst.* **1987**, *151*, 417–424.
(37) Fournier, J.B.; Dozov, I.; Durand, G. *Phys. Rev.* **1990**, *A41*, 2252–2255.

(38) Williams, C.E.; Kleman, M. *J. de Physique* **1975**, *36*, C1-315–320.

(39) Blanc, C.; Kleman, M. *Eur. Phys. J.* **1999**, *B10*, 53–60.

(40) Boltenhagen, P.; Lavrentovich, O.D.; Kleman, M. *J. Phys. II* **1994**, 4, 1439–1439.

(41) Fukuda, A.; Ouchi, Y.; Arai, H.; Takano, H.; Ishikawa, K.; Takezoe, H. *Liq. Cryst.* **1989**, *5*, 1055–1073.

(42) Perez, A.; Brunet, M.; Parodi, O. *J. de Physique Lett.* **1978**, *39*, 353–357.

(43) Bouligand, Y.; Kleman, M. *J. de Physique*, **1979**, *40*, 79.

(44) Bourdon, L.; Sommeria, J.; Kleman, M. *J. de Physique* **1982**, *43*, 77–96.

(45) Sethna, J.P.; Kleman, M. *Phys. Rev.* **1982**, *A26*, 3037–3040.

(46) Fournier, J.B.; Durand, G. *J. Phys. II* **1991**, *1*, 845–870.

(47) Bramley, J.P.; Evans, S.D.; Henderson, J.R.; Atherton, T.J.; Smith, N.J. *Liq. Cryst.* **2007**, *34*, 1137–1140.

(48) Guo, W.; Herminghaus, S.; Bahr, C. *Langmuir* **2008**, *24*, 8174–8180.

(49) Choi, M.C.; Pfohl, T.; Wen, Z.; Kim, M.W.; Israelachvili, J.N.; Safinya, C.R. *Proc. Natl. Acad. Sci.* **2004**, *101*, 17340–17344.

(50) Shojaei-Zadeh, S.; Anna, S.L. *Langmuir* **2006**, 22, 9986–9993.

(51) Yoon, D.K.; Choi, M.C.; Kim, Y.H.; Kim, M.W.; Lavrentovich, O.D.; Jung, H.T. *Nature Materials*, **2007**, *6*, 866–870.

(52) Kim, Y.H.; Yoon, D.K.; Choi, M.C.; Jeong, H.S.; Kim, M.W.; Lavrentovich, O.D.; Jung, H.T. *Langmuir* **2009**, *25*, 1685–1691.

(53) Reznikov, M.; Wall, B.; Handschy, M.A.; Bos, P.J. *J. Appl. Phys.* **2008**, *104*, 044902.

(54) Ponsinet, V.; Fabre, P.; Veyssié, M. *Europhys. Lett.* **1995**, *30*, 277–282.

(55) Li, Z.; Lavrentovich, O.D. *Phys. Rev. Lett.* **1994**, *73*, 280–283.

(56) Findon, A.; Gleeson, H.; Lydon, J. *Phys. Rev.* **2000**, *E 62*, 5137–5142.

(57) Garg, S.; Purdy, K.; Bramley, E.; Smalyukh, I.I.; Lavrentovich, O.D. *Liq. Cryst.* **2003**, *30*, 1377–1390.

(58) Yang, D.K.; Wu, S.T. *Fundamentals of Liquid Crystal Devices*; John Wiley: NY, 2006.

(59) Lavrentovich, O.D.; Kleman, M. *Phys. Rev.* **1993**, *E48*, R39–R42.

(60) Lavrentovich, O.D.; Kleman, M.; Pergamenshchik, V.M. *J. Phys. II* **1994**, *4*, 377–404.

(61) Poulin, P.; Stark, H.; Lubensky, T.C.; Weitz, D.A. *Science* **1997**, *275*, 1770–1773.

(62) Voloschenko, D.; Pishnyak, O.P.; Shiyanovskii, S.V.; Lavrentovich, O.D. *Phys. Rev.* **2002**, *E65*, 060701.

(63) Blanc, C.; Kleman, M. *Eur. Phys. J.* **2001**, *E4*, 241–251.

(64) Bellare, J.R.; Davis, H.T.; Miller, W.G.; Scriven, L.E. *J. Colloid Interface Sci.* **1990**, *136*, 305–326.

(65) Smalyukh, I.I.; Shiyanovskii, S.V.; Lavrentovich, O.D. *Chem. Phys. Lett.* **2001**, *336*, 88–96.

(66) Smalyukh, I.I.; Pratibha, R.; Madhusudana, N.V.; Lavrentovich, O.D. *Eur. Phys. J.* **2005**, *E16*, 179–191.

(67) Buyuktanir, E.A.; Zhang, K.; Gericke, A.; West, J.L. *Mol. Cryst. Liq. Cryst.* **2008**, *487*, 39–51.

(68) Evans, C.L.; Xie, X.S. *Annu. Rev. Anal. Chem.* **2008**, *1*, 883–909.

(69) Saar, B.G.; Park, H.-S.; Xie, X.S.; Lavrentovich, O.D. *Optics Express* **2007**, *15*, 13585–13586.

(70) Kachynski, A.V.; Kuzmin, A.N.; Prasad, P.N.; Smalyukh, I.I. *Appl. Phys. Lett.* **2007**, *91*, 151905.

(71) Iida, A.; Takanishi, Y. *Liq. Cryst.* **2007**, *34*, 1285–1290.

(72) Subacius, D.; Voloschenko, D.; Bos, P.; Lavrentovich, O.D. *Liq. Cryst.* **1999**, *26*, 295–298.

(73) Iwashita Y.; Tanaka, H. *Phys. Rev. Lett.* **2007**, *98*, 145703–4.

(74) DiDonna B.A.; Kamien, R. *Phys. Rev. Lett.* **2002**, *89*, 215504; *Phys. Rev.* **2003,** *E68*, 041703.

(75) Meyer, C.; Asnacios, S.; Kleman. M. *Eur. Phys. J.* **2001**, *E6*, 245–253.

(76) Blanc, C.; Zuodar, N.; Lelidis, I.; Kleman, M.; Martin. J.-L. *Phys. Rev.* **2004**, *E69*, 011705–3.

(77) Blanc, C.; Meyer, C.; Asnacios, S.; Lelidis, I.; Kleman, M.; Martin, J.-L. Phil. *Mag. Lett.* **2004**, *85*, 641–648.